The Journal of Chemical Physics

Highly accurate experimentally determined energy levels of H_3^+

Cite as: J. Chem. Phys. **150**, 214303 (2019); https://doi.org/10.1063/1.5099454
Submitted: 10 April 2019 . Accepted: 08 May 2019 . Published Online: 04 June 2019

Charles R. Markus, and Benjamin J. McCall

The Journal of Chemical Physics ARTICLE scitation.org/journal/jcp

Highly accurate experimentally determined energy levels of H_3^+

Cite as: J. Chem. Phys. 150, 214303 (2019); doi: 10.1063/1.5099454
Submitted: 10 April 2019 • Accepted: 8 May 2019 •
Published Online: 4 June 2019

Charles R. Markus and Benjamin J. McCall[a)]

AFFILIATIONS

Department of Chemistry, University of Illinois, 600 South Mathews Ave., Urbana, Illinois 61801, USA

[a)]Electronic mail: bjmccall@illinois.edu.

ABSTRACT

A sub-Doppler rovibrational spectroscopic survey of H_3^+ has been conducted which included 36 transitions in the $\nu_2 \leftarrow 0$ fundamental band, 15 transitions in the $2\nu_2^2 \leftarrow \nu_2$ hot band, and 7 transitions in the $2\nu_2^2 \leftarrow 0$ overtone band, improving the uncertainties of most transitions by more than an order of magnitude to ~4 MHz. Combination differences were used to determine relative energy levels and forbidden rotational transitions up to $J = 6$. A fit of the ground state to an effective Hamiltonian was used to connect *ortho* and *para* states, and to determine the absolute energy levels relative to the forbidden (0, 0) state. Ultimately, 62 rovibrational energy levels in the ground, ν_2, and $2\nu_2^2$ states were determined with ~10 MHz uncertainty. Comparing the experimentally determined energy levels with *ab initio* calculations revealed an unexpected dependence of the residuals on the quantum number G.

I. INTRODUCTION

H_3^+ is the simplest polyatomic molecule, and calculations of its rovibrational energy levels have been a useful test for state-of-the-art *ab initio* calculations.[1] For astronomers, observations of H_3^+ have allowed for probing conditions in a range of environments from molecular clouds to the ionospheres of gas giants.[2,3] Astronomers and theoreticians rely on laboratory measurements for accurate and precise transition frequencies, while experimentalists have relied on theorists to understand and assign the spectrum of H_3^+ as they have moved to higher vibrational quanta.

Highly accurate calculations of H_3^+ must go beyond the clamped nuclei Born–Oppenheimer approximation. The accurate potential energy surface (PES) calculated by Pavanello *et al.*[4] included corrections for relativistic effects and adiabatic coupling between electronic and nuclear motion, and was able to reproduce rovibrational transitions to within 0.2 cm^{-1}, even for states beyond the barrier to linearity (~10 000 cm^{-1}). The accuracy of H_3^+ calculations is currently limited by treatment of the nonadiabatic coupling, where electronic motion changes the effective mass of the nuclei.[5] To account for this, Diniz *et al.*[6] calculated coordinate-dependent masses and were able to achieve agreement with high-precision rovibrational transition frequencies on the order of 0.001 cm^{-1}, after empirical scaling of the mass surfaces. As the accuracy of *ab initio* calculations continues to approach experimental uncertainties, there is a need for improved experimentally determined transition frequencies and absolute energy levels.

A few spectroscopic techniques have demonstrated the ability to measure rovibrational transition frequencies of H_3^+ with megahertz-level uncertainty, all of which have relied on optical frequency combs (OFCs) for accurate frequency calibration. Laser-induced reaction spectroscopy on ions in a 4 K ion trap was able to measure low-lying rotational transitions of H_3^+ and isotopologues with sub-megahertz uncertainties.[7] However, due to the low temperature of the trap and the large rotational constants of H_3^+, only the lowest rotational states were accessible. Other experiments have utilized sub-Doppler spectroscopy of H_3^+ ions generated in normal glow discharges, which can access higher rotational states. The first published sub-Doppler measurements of H_3^+ used a double-pass pump-probe scheme with wavelength modulation on an extended negative glow discharge cell.[8] However, issues with the frequency calibration were later found,[7,9] which were resolved with a new double pass spectrometer which used an intensity modulated pump and a new scheme for frequency calibration.[10] In the past, we have demonstrated that the technique Noise

Immune Cavity Enhanced Optical Heterodyne Velocity Modulation Spectroscopy (NICE-OHVMS)[11] is capable of determining rovibrational transition frequencies with megahertz-level uncertainty.[9,12] To date, 24 rovibrational transition frequencies have been measured with megahertz-level uncertainty or better, all of which are from the $\nu_2 \leftarrow 0$ band and all but four of which are from the R branch.

In this study, NICE-OHVMS has been used to measure rovibrational transitions of H_3^+ in a positive column discharge cell, and an OFC was used for accurate frequency calibration. We have measured 36 transitions in the $\nu_2 \leftarrow 0$ band spanning the P, Q, and R branches, 15 transitions in the $2\nu_2^2 \leftarrow \nu_2$ hot band, and 7 transitions in the $2\nu_2^2 \leftarrow 0$ overtone band of H_3^+, improving the uncertainties to ~4 MHz, which for most transitions is an improvement by a factor of 40 or more. These new data have been used to significantly improve predictions of forbidden rotational transitions and to determine absolute rovibrational energy levels.

A. H_3^+ structure and notation

H_3^+ is an oblate symmetric top and has the equilibrium geometry of an equilateral triangle belonging to the point group D_{3h}. It has two vibrational modes: the infrared inactive symmetric stretch ν_1 and the doubly degenerate infrared active stretch ν_2. The degeneracy of the ν_2 mode leads to vibrational angular momentum l, and the standard notation for a vibrational state with vibrational quanta ν_2 in the ν_2 mode is $\nu_2 v_2^l$. For vibrationally excited states, k and l are not good quantum numbers due to strong l-resonance, and it is useful to define the better quantum number $g \equiv k - l$.[13] In cases where two combinations of k and l can produce the same $G = |g|$, the states are labeled with a u or l for the upper and lower levels, respectively. Similar to standard symmetric top labeling, the notation for rotational states is $(J, G)u|l$. Additional information on the notation can be found in the comprehensive evaluation of H_3^+ spectroscopy by Lindsay and McCall.[14]

The three protons are identical Fermions and must adhere to the Pauli principle. Under the three-particle permutation-inversion group S_3^*, the total wavefunction must be antisymmetric upon the exchange of two nuclei (12) and symmetric upon a cyclic (123) permutation. For *ortho* states, where the nuclear spin $I = 3/2$, only states with $G = 3n$ have the Pauli allowed symmetry, where n is an integer ≥ 0. The remaining *para* states with $I = 1/2$ will follow $G = 3n \pm 1$. Additionally, in the ground vibrational state, when $G = 0$ only states with odd J values have the proper symmetry. Notably, the lowest rotational state (0, 0) does not exist.

Important selection rules to consider for rovibrational transitions are $\Delta J = 0, \pm 1$, Δk is odd, and $\Delta g = 3n$. Because Δk must be odd, it follows that hot band and fundamental band transitions with $\Delta l = \pm 1$ must follow $\Delta g = 0$, and overtone transitions with $\Delta l = \pm 2$ follow $\Delta g = \pm 3$. Transitions are labeled with the usual P, Q, and R to indicate ΔJ, with the inclusion of a superscript t or n if $\Delta g = +3$ or -3, respectively, and a final superscript u or l when it is necessary to indicate the final state.

These selection rules can be used to our advantage for experimentally determining energy levels in the ground state. If two transitions share a final state, the difference in their frequencies provides an energy level spacing between their initial states, which is called a ground state combination difference (CD). The selection rule $\Delta G = 0$ for fundamental band transitions means that they can only connect states with the same G value. Connecting different G ladders is possible using $2\nu_2^2 \leftarrow 0$ overtone transitions with the selection rule $\Delta G = \pm 3$. Then, fundamental and hot band transitions can be used to complete the CD by connecting the ground to the $2\nu_2^2$ state.

Because transitions between *ortho* and *para* states are strictly forbidden, CDs are only able to determine energy levels relative to the lowest *ortho* or *para* levels. Connecting the *ortho* and *para* manifolds and determining energy levels relative to the forbidden (0, 0) state require additional analysis using an effective Hamiltonian or empirically scaled numerical calculations.

II. EXPERIMENTAL

A. Spectrometer

All data were collected with our NICE-OHVMS spectrometer, and the configuration for measurements from 3.2 to 3.9 μm has been described in detail previously.[9] In brief, tunable 1064 nm light from a distributed feedback laser is passed through a fiber coupled proton-exchanged electro-optic modulator (EOM). The EOM phase modulates the light both at the heterodyne detection frequency to generate a frequency modulation (FM) triplet and at ~4 MHz for Pound-Drever-Hall (PDH) locking.[15] The light is then amplified by a ytterbium doped fiber amplifier to 10 W. This is sent to a commercial optical parametric oscillator (OPO, Aculight Argos 2400 SF) which generates the signal and idler beams with up to 1 W of power. For the fundamental and hot band measurements, the idler beam from a signal-resonant C (3.2–3.9 μm) or D (3.9–4.6 μm) module was used for spectroscopy. For the overtone transitions, the signal beam from an idler-resonant A module (1.96–2.01 μm) was used.

There are a number of challenges for using an OPO with a periodically poled lithium niobate (PPLN) crystal at wavelengths longer than 3.9 μm. As the wavelength increases from 3.9 μm, multiphonon absorption causes the output power to decline, with only ~30 mW of idler available near 4.51 μm. In addition, at idler wavelengths of 3.96–4.03 μm, PPLN has an OH absorption at the signal wavelength which leads to significantly higher threshold power. There are also a number of "blind spots" with little-to-no output power due to absorption from H_2O or CO_2 within the OPO cavity. In regions where the threshold power was too high, the mode-selecting etalon within the OPO cavity was removed. This significantly reduced the threshold power but also led to problems with multimode behavior and rapid frequency drift. Single-mode operation was achieved by setting the pump power just above threshold, which also resulted in less idler power. The frequency was stabilized by locking the signal beam to an OFC, which is described in Sec. II B.

The beam which was used for spectroscopy was locked onto resonance of an external cavity (finesse 100–400) using a PDH locking scheme. In order to generate the PDH error signal, the light reflected off the first cavity mirror was picked off with a CaF_2

window and focused onto a fast mid-IR detector. Slow PDH corrections (<100 Hz) were sent to piezoelectric transducers (PZTs) on both of the cavity mirrors, and fast corrections were sent to a fiber coupled acousto-optic modulator (AOM) on the seed laser. Brewster-plate spoilers[16,17] were set before and after the cavity to average out signals from parasitic etalons. The heterodyne frequency was set to 77 or 231 MHz to be an integer multiple of the free spectral range (FSR) of the cavity (77 MHz) in order to couple the FM sidebands into cavity modes on either side of the carrier.

A triple-jacketed liquid-cooled discharge cell, "Black Widow,"[18] was used to generate the H_3^+ ions and was placed within the external cavity. The ends of the cell were sealed with Brewster windows, and a mixture of H_2 and He gas was flowed through the cell. Electrodes at the ends of the cell were driven by a 2 kV sinusoidal voltage to generate a discharge. The discharge was cooled by flowing chilled water or liquid nitrogen around the jacket surrounding the cell, depending on the desired rotational temperature.

The detector scheme depended on the wavelength of light being used for spectroscopy. For measurements from 3.2 to 4.6 μm, fast thermoelectrically cooled HgCdTe detectors (Boston Electronics Vigo PVI-4TE-6) were used for generating the PDH error signal and measuring the light transmitted from the cavity. To avoid saturating the detector, a fraction of the light was picked off, further attenuated to <500 μW, and focused onto the detector. For measurements near 2 μm, fast liquid nitrogen cooled InSb detectors (Kolmar, KISDP-0.1) were used instead.

The output of the transmission detector was sent to a pair of radio frequency (RF) mixers set 90° out of phase with each other in order to recover the in-phase and quadrature components of the heterodyne signal. The mixer outputs were low-pass filtered and sent to a pair of dual-channel lock-in amplifiers referenced to twice the velocity modulation frequency to recover the in-phase and quadrature components of the velocity modulation signal. This results in four total channels of detection. The lock-in amplifiers were set to a 300 ms time constant, and scans were taken by stepping the frequency in 3 MHz steps and holding for 2 s at each point.

B. Frequency calibration

A Global Positioning System (GPS) referenced OFC (Menlo Systems FC-1500, 100 MHz repetition rate) which spans 1050–2100 nm was used to accurately calibrate the frequency while spectra were recorded. For wavelengths between 3.2 and 4.6 μm, the idler frequency was determined indirectly by taking the difference between the pump and signal frequencies. The pump and signal beats were generated using free-space optics, as described previously.[9] The integer number of comb modes between the pump and signal was determined by taking a rough measurement of the idler frequency with a mid-IR wavemeter (Bristol 621). The beat generated between the signal and the nearest comb tooth was locked at 20 MHz using a phase-locked loop (PLL) with corrections sent to a PZT on the OPO signal cavity, which also acted to stabilize the idler frequency. Because the pump frequency steps in 3 MHz increments during a scan, a double-pass AOM was used to keep the beat frequency within a 30 MHz bandpass using a feed-forward scheme.[19] When the AOM reached the end of its diffraction efficiency, it shifted the pump 100 MHz to the next comb tooth. A delay of 2 s after each step ensured the frequency counters had time to measure both beat frequencies. The frequency of the idler can then be determined by

$$\nu_{idler} = \Delta n \times f_{RR} \pm f_{pb} \mp f_{sb} - 2 \times f_{AOM},$$

where Δn is the number of comb modes between the pump and signal frequencies, f_{RR} is the repetition rate of the comb, f_{pb} and f_{sb} are the frequencies of the pump and signal beats, respectively, and f_{AOM} is the frequency applied to the AOM. The sign of the beat notes represents whether the frequency of the beam was above or below the nearest comb tooth, which can be determined by applying a small step to the repetition rate of the OFC and observing the change in the beat frequency. The accuracy of the frequency calibration was found to be ~160 kHz using standard transitions of methane.[19]

For measurements at 2 μm, the wavelength of the signal beam was within the coverage of the OFC and could be measured directly and calculated using the following equation:

$$\nu_{signal} = n \times f_{RR} \pm f_{CEO} \pm f_{sb},$$

where n is the integer mode number of the nearest comb tooth and f_{CEO} is the carrier envelope offset (CEO) frequency. The mode number of the nearest comb tooth can be determined by measuring the signal with the wavemeter. The CEO was locked at 20 MHz using a PLL.

To generate the beat between the signal and the comb, they were overlapped using fiber optics, which offers superior spatial overlap compared to free space methods. First, a fraction of the signal beam was picked off before the external cavity and fiber coupled. The polarization of the light was controlled using a fiber optic paddle polarizer (Thorlabs FPC024) before being sent into one input of a 2 × 2 fiber optic coupler (Thorlabs TW2000R5A2B). The OFC was also fiber coupled and sent into the other input of the 2 × 2 coupler. One of the outputs of the coupler was sent into free space, reflected off of a grating, and focused onto a fast liquid nitrogen cooled InSb detector (Kolmar KISDP-0.5). The beat frequency was locked at 20 MHz using a frequency-to-voltage converter with corrections sent to the PZT driver that controlled the seed laser of the OPO. The frequency of the signal beam was scanned in 3 MHz steps by stepping the repetition rate of the comb, which allowed for ~400 MHz of scanning.

III. RESULTS

An example of a NICE-OHVMS scan of the $Q(1, 0)$ transition in the $\nu_2 \leftarrow 0$ fundamental band is shown in Fig. 1. The left and right plots represent the in-phase and quadrature components of the heterodyne signal, and the red and blue traces represent the in-phase and quadrature components of the velocity modulation signal. The Doppler profile appears as a wide derivative line shape, while the narrower feature at the center is a set of Lamb dips separated by half integer multiples of the heterodyne frequency. Due to the large homogeneous broadening of approximately 80 MHz, these features overlapped when the heterodyne frequency was 77 MHz and were resolved when it was 231 MHz.[16]

The line center is determined by fitting the sub-Doppler feature in all four channels simultaneously using a global least-squares fitting routine, where the center frequency is a shared parameter.[9] In

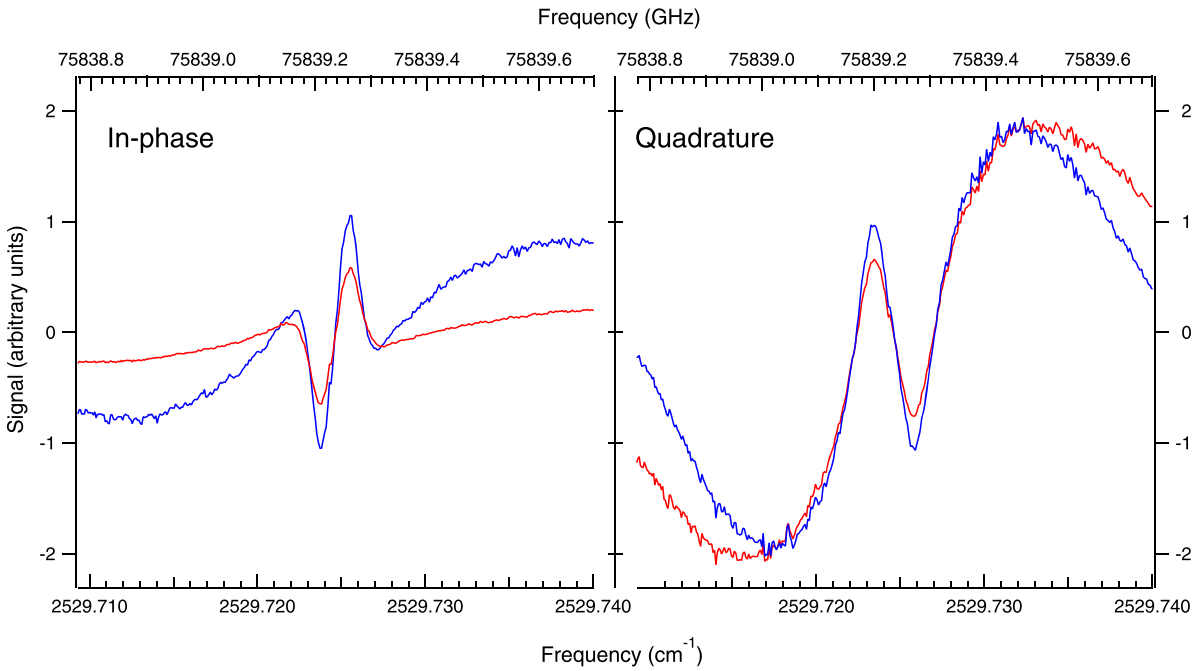

FIG. 1. A NICE-OHVMS scan of the Q(1, 0) transition in the $\nu_2 \leftarrow 0$ fundamental band, recorded with a 77 MHz heterodyne modulation frequency. The left and right plots represent the in-phase and quadrature components of the heterodyne signal, while the red and blue traces represent the in-phase and quadrature components of the velocity modulation signal.

the past, the uncertainty was reported as the standard deviation of a set of at least five scans and ranged from 700 kHz to 2.5 MHz with most having an uncertainty of ~1 MHz.[9,12]

When NICE-OHVMS was used to investigate the $\nu_1 \leftarrow 0$ fundamental band of D_2H^+, problems with the line center determination were discovered.[20] Disagreements with the values reported by Jusko *et al.*[7] were as large as 4 MHz, well outside of our measured uncertainty. Remeasuring transitions on multiple days revealed day-to-day changes of up to 6 MHz, although the disagreement with the previous values never exceeded 4 MHz. To verify that the OFC calibration was not causing the issue, standard methane transitions were measured using sub-Doppler spectroscopy, and the line center frequencies agreed within 200 kHz with an root-mean-square (rms) error of 160 kHz.[19]

The origin of the disagreement was determined to be asymmetry in the Doppler profile, where one lobe was diminished relative to the other, giving the appearance that the Lamb dip was sitting nearer to the top or bottom of the profile. The asymmetry along with the offset would change with small adjustments to the alignment of the beam to the cavity. The cause of this effect has not yet been determined, but the error was contained within 4 MHz when the alignment to the cavity was optimized. The disagreement with values reported by Jusko *et al.* was distributed with an rms error of 2.3 MHz, and an estimated uncertainty of 4 MHz has been applied for our H_3^+ NICE-OHVMS measurements to give a conservative estimate of the error which encapsulates the asymmetry offsets. Examples showing this effect are available in the supplementary material.

A. Fundamental band $\nu_2 \leftarrow 0$

To measure transitions in the ν_2 fundamental band, H_3^+ ions were generated in a discharge of 300 mTorr of H_2, with either liquid nitrogen or chilled water flowing through the jacket surrounding the cell. Liquid nitrogen cooling was used for transitions starting from states with $J < 3$, which resulted in a rotational temperature of ~170 K. Transitions that started from higher rotational levels were observed with chilled water as the coolant, which gave a rotational temperature of ~450 K.

Previously, NICE-OHVMS was used to measure 20 *R* branch transitions spanning $R(1,1)^l$ to $R(4,1)^u$.[9,12] Changes to the instrument allowed this to be expanded. The introduction of Brewster-plate spoilers significantly improved the sensitivity of the instrument by avoiding parasitic etalons, allowing for weaker transitions to be measured.[16] In addition, a set of high reflectivity mirrors which covered 3.7–4.77 μm (Layertec, 99% reflectivity) were acquired, which extended the coverage of the instrument to include *Q* and *P* branch transitions. Additionally, locking the signal frequency to the comb enabled stable operation of the D module (3.9–4.6 μm) and made measurements of many *Q* branch and *P* branch transitions possible.

With these changes, an additional 36 transitions have been measured from $P(4, 4)$ to $R(4,4)^u$ with an estimated uncertainty of 4 MHz. It should be noted that 18 of the transitions from the current study were presented at the International Symposium on Molecular Spectroscopy.[21,22] The new transition frequencies are listed in Table I with comparisons to the most recent literature values. The

TABLE I. Newly measured rovibrational transitions in the $\nu_2 \leftarrow 0$ fundamental band with comparison to previous values. All units are in MHz, and uncertainties are given in parentheses in units of the least significant digit.

Transition	Frequency (this work)	Frequency (previous)	Difference
$P(4, 4)$	66 477 520.51(400)	66 477 509(120)[24]	11.51
$P(4, 3)$	66 497 862.13(400)	66 497 835(120)[24]	27.13
$P(4, 1)^u$	66 850 568.90(400)	66 850 570(120)[24]	−1.10
$P(3, 3)$	68 920 206.83(400)	68 920 188(120)[24]	18.83
$Q(6, 5)^l$	73 348 494.68(400)	73 348 182(120)[24]	312.68
$Q(6, 3)^l$	73 530 562.21(400)	73 530 636(120)[24]	−73.79
$Q(6, 4)^l$	73 551 669.33(400)	73 551 321(120)[24]	347.33
$P(1, 1)$	73 667 685.63(400)[21]	73 667 701(150)[23]	−15.37
$Q(5, 4)^l$	73 975 496.87(400)	73 975 378(90)[25]	118.87
$Q(5, 0)$	74 106 385.57(400)	74 106 387(90)[25]	−1.43
$Q(5, 1)^l$	74 118 638.05(400)	74 118 439(120)[24]	199.05
$Q(5, 3)^l$	74 134 186.83(400)	74 134 058(120)[24]	128.83
$Q(5, 2)^l$	74 145 994.94(400)	74 145 810(120)[24]	185.94
$Q(4, 3)^l$	74 545 148.64(400)	74 545 163(150)[23]	−14.36
$Q(4, 2)^l$	74 700 633.00(400)	74 700 636(150)[23]	−3.00
$Q(4, 1)^l$	74 724 417.54(400)	74 724 379(150)[23]	38.54
$Q(3, 0)$	75 220 254.22(400)	75 220 266(150)[23]	−11.78
$Q(2, 1)^l$	75 494 063.34(400)[21]	75 494 067(150)[23]	−3.66
$Q(1, 0)$	75 839 225.87(400)[21]	75 839 225.64(85)[10]	0.23
$Q(1, 1)$	76 309 753.78(400)[21]	76 309 754.18(93)[10]	−0.04
$Q(2, 1)^u$	76 536 660.62(400)	76 536 655(150)[23]	5.62
$Q(2, 2)$	76 586 944.78(400)[21]	76 586 946.28(158)[10]	−1.50
$Q(3, 3)$	76 791 725.52(400)[21]	76 791 723.23(255)[10]	2.29
$Q(3, 2)^u$	76 879 298.48(400)[22]	76 879 318(150)[23]	−19.52
$Q(4, 4)$	76 965 382.04(400)[22]	76 965 358(150)[23]	24.04
$Q(3, 1)^u$	77 007 873.75(400)[22]	77 007 929(150)[23]	−55.25
$Q(4, 3)^u$	77 186 330.11(400)[22]	77 186 335(150)[23]	−4.89
$Q(5, 4)^u$	77 381 778.20(400)[22]	77 381 950(120)[24]	−171.80
$Q(4, 2)^u$	77 433 718.54(400)[22]	77 433 721(300)[25]	−2.46
$Q(6, 5)^u$	77 555 627.17(400)[22]	77 555 859(120)[24]	−231.83
$Q(5, 3)^u$	77 750 464.98(400)[22]	77 749 975(120)[24]	490.98
$R(3, 1)^l$	84 881 719.64(400)[22]	84 881 438(300)[26]	281.64
$R(4, 2)^l$	86 696 143.62(400)[22]	86 695 992(300)[26]	152.47
$R(5, 3)^l$	88 425 484.47(400)	88 425 434(120)[24]	50.11
$R(5, 4)^l$	88 593 414.11(400)[22]	88 593 288(300)[27]	125.71
$R(4, 4)^u$	90 180 929.71(400)[22]	90 180 933.3(39)[10]	−3.59

measurements by McKellar and Watson[23] using absorption Fourier transform infrared (FTIR) spectroscopy compare extraordinarily well, with an average offset of 3 MHz, and an rms error of only 20 MHz, despite their claimed uncertainties of 150 MHz. Values measured using emission FTIR[24] compare less favorably, with an average offset of 75 MHz and an rms error of 170 MHz, which is larger than the estimated uncertainty of 120 MHz. Emission spectroscopy of H_3^+ is difficult in this region, due to interference from H_2 electronic transitions, which could explain the understated uncertainty. Additionally, the 5 transitions from the literature which were measured with megahertz-level uncertainty[10] agreed with the new values within our estimated uncertainty of 4 MHz.

B. Hot band $2\nu_2^2 \leftarrow \nu_2$

To observe transitions in the $2\nu_2^2 \leftarrow \nu_2$ hot band, the H_3^+ ions needed to be vibrationally hot yet rotationally cold. The addition of a He buffer gas, which has a higher ionization energy than H_2, increases the electron temperature of the plasma which results in a higher vibrational temperature.[25] For all of our hot band

measurements, the gas mixture was 300 mTorr of H_2 and 2 Torr of He. Liquid nitrogen was flowed around the cell, which was able to rotationally cool the ions without significantly affecting the vibrational temperature. This is because collisions are more efficient at rotational cooling than vibrational cooling.[28]

Higher pressures will increase the power required to saturate a transition and observe a Lamb dip, and we found that we were still able to saturate transitions with the 2 Torr of He buffer gas. An example of the $R(2, 0)$ hot band transition is shown in Fig. 2. To our knowledge, these are the first sub-Doppler measurements of H_3^+ hot band transitions. It appears that the He buffer gas may also have led to higher translational temperatures, causing larger Doppler broadening.

Overall, 15 transitions in the $2\nu_2^2 \leftarrow \nu_2$ band from $Q(2, 0)$ to $R(4, 0)$ were measured with an estimated uncertainty of 4 MHz. The results can be found in Table II with comparisons to measurements by Bawendi *et al.*[25] The previous values are systematically lower by an average of 97 MHz, and all but 6 are outside of one standard deviation. This is consistent with other studies from the Oka group during this time, when scanning rates were too rapid for the lock-in time constants. This led to "line dragging" that resulted in a systematic offset in the reported frequencies. For this reason, Lindsay and McCall recommended an increased uncertainty of 300 MHz for this and other works from the Oka group during this time.[14]

C. Overtone band $2\nu_2^2 \leftarrow 0$

To extend the coverage of the NICE-OHVMS instrument to include the $2\nu_2^2 \leftarrow 0$ overtone band at 2 μm, high reflectivity mirrors which covered 1.92–2.18 μm (Layertec, 99.0% reflectivity) were used for the NICE-OHVMS cavity. The H_3^+ ions were generated in a discharge of 300 mTorr of H_2, and because all the desired transitions were from low lying rotational states only liquid nitrogen cooling was used.

TABLE II. Newly measured rovibrational transitions in the $2\nu_2^2 \leftarrow \nu_2$ hot band with comparison to previous values. All units are in MHz, and the uncertainties are given in parentheses in units of the least significant digit.

Transition	Frequency (this work)	Frequency (previous)[25]	Difference
$Q(2, 0)$	74 170 467.71(400)	74 170 273(90)	194.71
$Q(1, 2)$	76 130 916.62(400)	76 130 826(90)	90.62
$Q(3, 0)$	76 190 405.61(400)	76 190 245(90)	160.61
$Q(2, 2)$	76 221 275.11(400)	76 221 243(90)	32.11
$Q(3, 3)$	76 575 377.32(400)	76 575 268(90)	109.32
$Q(3, 4)$	77 338 982.2(400)	77 338 899(90)	83.20
$Q(4, 4)$	77 441 047.83(400)	77 441 039(90)	8.83
$Q(5, 5)$	77 924 189.92(400)	77 924 094(90)	95.92
$R(0, 1)$	78 062 541.75(400)	78 062 448(90)	93.75
$Q(5, 0)$	79 405 938.33(400)	79 405 789(90)	149.33
$R(1, 0)$	80 051 627.89(400)	80 051 601(90)	26.89
$R(1, 2)$	81 491 483.59(400)	81 491 445(90)	38.59
$R(2, 0)$	82 578 971.99(400)	82 578 882(90)	89.99
$R(3, 4)$	87 928 908.53(400)	87 928 768(90)	140.53
$R(4, 0)$	88 283 855.00(400)	88 283 722(90)	133.00

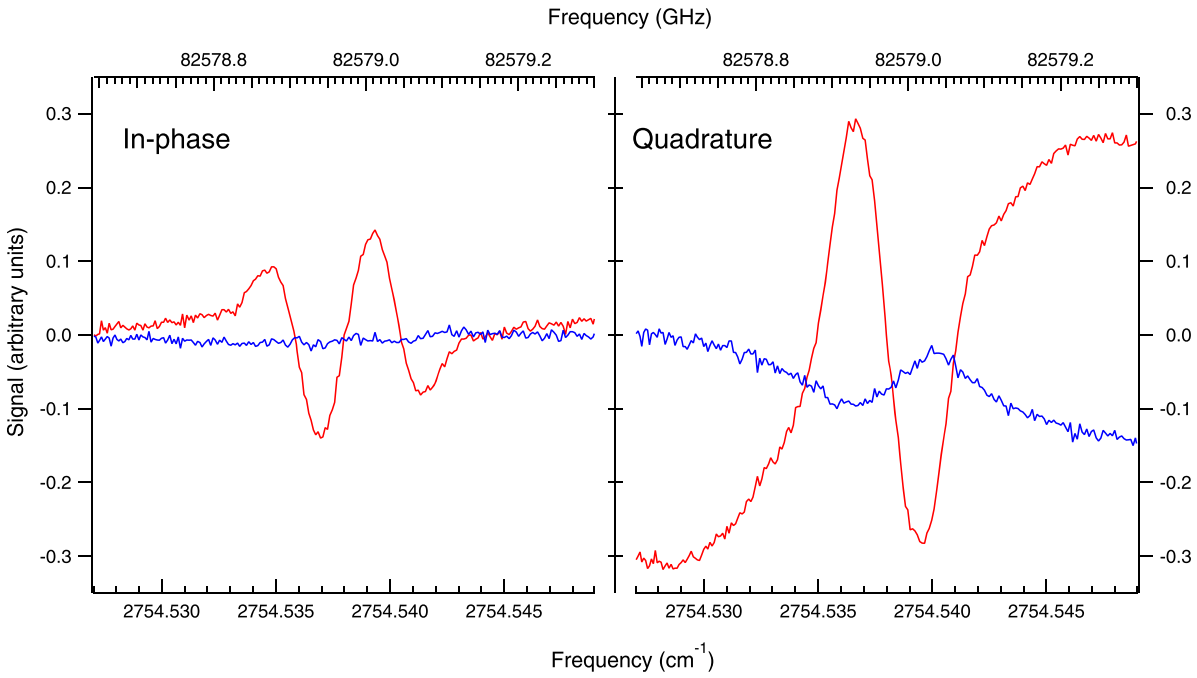

FIG. 2. A NICE-OHVMS scan of the $R(2, 0)$ transition in the $2\nu_2^2 \leftarrow \nu_2$ hot band. The left and right plots represent the in-phase and quadrature components of the heterodyne signal, while the red and blue traces represent the in-phase and quadrature components of the velocity modulation signal.

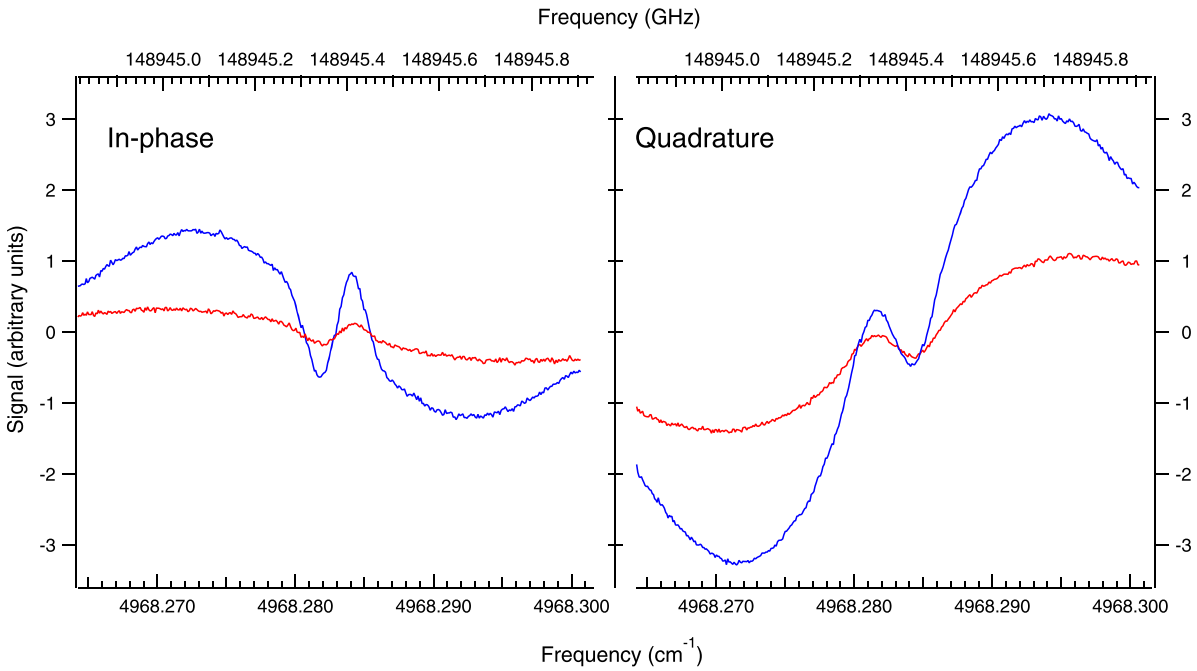

FIG. 3. A NICE-OHVMS scan of the ${}^tR(1, 1)$ transition in the $2\nu_2^2 \leftarrow 0$ overtone band. The left and right plots represent the in-phase and quadrature components of the heterodyne signal, while the red and blue traces represent the in-phase and quadrature components of the velocity modulation signal.

The large anharmonicity of the H_3^+ potential leads to strong overtone transitions, and the $2\nu_2^2 \leftarrow 0$ band is no exception with 1/7 the intensity of the $\nu_2 \leftarrow 0$ fundamental band.[29] Despite the transition dipole moment being smaller, it was found that the instrument was still capable of saturating transitions to generate strong sub-Doppler features, and an example of the ${}^tR(1, 1)$ overtone transition is shown in Fig. 3. To our knowledge, these are the first sub-Doppler measurements of H_3^+ overtone transitions.

Ultimately, 7 transitions were measured from ${}^tR(1, 1)$ to ${}^tR(1, 0)$. We were unable to measure transitions below ${}^tR(1, 1)$ since the OPO would become unstable when tuned below 4950 cm^{-1}. The results can be found in Table III with comparison to measurements by Xu *et al.*[30] The previous values displayed an even larger systematic offset than the hot band measurements by Bawendi *et al.*,[25] with all transitions being outside of their estimated uncertainty of 150 MHz with an average offset of 225 MHz. It is likely that the measurements suffered from the same systematic error due to scanning too rapidly.

TABLE III. Newly measured rovibrational transitions in the $2\nu_2^2 \leftarrow 0$ overtone band with comparison to previous values. All units are in MHz, and the uncertainties are given in parentheses in units of the least significant digit.

Transition	Frequency (this work)	Frequency (previous)[30]	Difference
${}^tR(1, 1)$	148 945 367.99(400)	148 945 047(150)	320.99
${}^nP(3, 3)$	149 043 829.87(400)	149 043 649(150)	180.87
${}^nQ(1, 1)$	150 600 776.89(400)	150 600 621(150)	155.89
${}^nQ(2, 1)$	150 767 979.04(400)	150 767 756(150)	223.04
${}^tR(3, 2)$	150 869 192.88(400)	150 868 966(150)	226.88
${}^tR(2, 1)$	151 751 556.50(400)	151 751 405(150)	151.50
${}^tR(1, 0)$	152 721 132.07(400)	152 720 814(150)	318.07

IV. DISCUSSION

A. Combination differences and forbidden rotational transitions

CDs are able to determine energy level spacings in the ground state and predict forbidden rotational transitions without the need of an effective Hamiltonian. The improved transition frequencies were used to calculate 21 CDs in the ground state with uncertainties of 4–8 MHz, which are presented in Table IV. The transitions which contributed to each CD are provided in the supplementary material. Different CDs which calculated the same energy level spacing were used to assess the estimated uncertainty of the NICE-OHVMS measurements. The differences between redundant CDs had an rms error of 4.7 MHz and a reduced rms of 0.72. This confirms that the estimated uncertainty of 4 MHz was sufficient, if not slightly overstated.

Calculating CDs between states with different G values is essential for predicting forbidden rotational transitions and for calculating absolute energy levels. This was made possible by the new measurements of overtone transitions which have the selection rule $\Delta G = \pm 3$, coupled with measurements of fundamental band and hot

TABLE IV. Ground state CDs of H_3^+. All frequencies are in MHz, and the uncertainties are given in parentheses in units of the least significant digit.

$(J', G') - (J'', G'')$	Energy difference
$\Delta G = 0$	
(2, 1) — (1, 1)	5 193 359.2(40)
	5 193 359.5(40)
(3, 1) — (2, 1)	7 716 972.8(56)
(3, 2) — (2, 2)	7 756 239.3(40)
(4, 1) — (3, 1)	10 157 302.1(56)
	10 157 304.8(56)
(4, 2) — (3, 2)	10 206 479.3(41)
	10 206 485.8(56)
(4, 3) — (3, 3)	10 293 857.6(41)
	10 293 861.1(47)
	10 293 864.3(40)
(5, 2) — (4, 2)	12 550 148.7(56)
(5, 3) — (4, 3)	12 644 246.8(56)
	12 644 254.4(41)
(5, 4) — (4, 4)	12 799 151.5(56)
	12 799 151.6(56)
(3, 0) — (1, 0)	12 888 688.8(69)
(6, 3) — (5, 3)	14 894 922.2(56)
(6, 4) — (5, 4)	15 041 744.8(56)
(6, 5) — (5, 5)	15 272 463.6(40)
(5, 0) — (3, 0)	22 615 726.8(80)
$\Delta G = 3$	
(2, 1) — (2, 2)	2 040 242.2(59)
(2, 2) — (1, 1)	3 153 122.9(81)
(3, 3) — (1, 0)	6 847 023.5(57)
(4, 4) — (2, 1)	7 935 052.8(69)
	7 935 052.5(89)

band transitions. With the new measurements, five CDs were calculated connecting states with $G = 0$ and 3, and $G = 1$, 2, and 4, which had uncertainties of 5.7–9.0 MHz. These values are also presented in Table IV.

The forbidden rotational transitions of H_3^+ have been predicted to be relatively strong, with transition dipole moments as large as 38 mD due to the significant centrifugal distortion.[31] The selection rules are $\Delta J = 0, \pm 1$ and $\Delta k = \pm 3$, and the transition frequencies can be predicted directly from CDs. Redundant CDs were averaged, and in cases where two different sets of CDs could calculate the same transition the average was used. This resulted in 16 predicted forbidden rotational transitions, with uncertainties of 7–14 MHz, which are presented in Table V.

Of particular interest to astronomers is the (4, 4) → (3, 1) forbidden rotational transition, which is well positioned to be an astrophysical maser.[32] The lifetime of the (4, 4) state is on the order of 10 years, while the (3, 1) state has a lifetime of less than 8 h.[31] This would lead to population inversion in an environment where there is sufficient excitation and limited collisional quenching. These conditions could be met in the molecular gas surrounding an active galactic nucleus or possibly in the ionospheres of gas giants. The uncertainty of the predicted frequency has been improved from 280 to 10 MHz, which greatly improves the prospects for an astronomical detection.

TABLE V. Predictions for forbidden rotational transitions of H_3^+, calculated from combination differences. All frequencies are in MHz, and the uncertainty is given in parentheses in units of the least significant digit.

$(J', G') - (J'', G'')$	Frequency
(4, 4) ← (3, 1)	218 079.7(89)
(3, 1) ← (3, 2)	2 000 972.8(103)
(2, 1) ← (2, 2)	2 040 239.3(76)
(5, 4) ← (4, 1)	2 859 927.8(120)
(2, 2) ← (1, 1)	3 153 120.0(95)
(4, 3) ← (3, 0)	4 252 195.7(72)
(3, 2) ← (2, 1)	5 716 000.0(93)
(5, 0) ← (5, 3)	5 719 280.4(137)
(3, 0) ← (3, 3)	6 041 665.2(90)
(4, 2) ← (3, 1)	8 205 509.7(115)
(6, 3) ← (5, 0)	9 175 641.9(131)
(3, 1) ← (2, 2)	9 757 212.1(95)
(4, 1) ← (4, 4)	9 939 223.8(106)
(5, 2) ← (4, 1)	10 598 354.9(140)
(4, 1) ← (3, 2)	12 158 276.3(118)
(5, 0) ← (4, 3)	18 363 531.0(128)

B. Absolute energy levels

For direct comparison with *ab initio* calculations, it is desirable to have experimentally determined energy levels relative to the (0, 0) state. However, this cannot be accomplished using CDs alone. The (0, 0) state is forbidden by the Pauli principle, and transitions between *ortho* and *para* states are strictly forbidden. Absolute energy levels can be determined by fitting the ground state to an effective Hamiltonian and then using the molecular constants to calculate the energy of the (1, 0) and (1, 1) states. Then, CDs can be used to fill out the rest of the energy levels. This strategy was used by Lindsay and McCall in their comprehensive review of H_3^+ spectroscopy,[14] and their values for the (1, 0) and (1, 1) energy levels have been used since.[33,34]

1. Determining molecular constants

H_3^+ suffers from severe centrifugal distortion, which makes it challenging to fit CDs or energy levels to an effective Hamiltonian. Our goal for determining the molecular constants of H_3^+ was to calculate the energies of the (1, 0) and (1, 1) states, and it was therefore of critical importance that the parameters were well behaved at low J. Including higher order parameters can lead to issues with the lower order terms, especially when there is lack of accurate experimental data at higher rotational levels. To avoid this, limited data sets were used for fitting in order to avoid the need of higher order parameters.

Fits were performed on energy levels relative to (1, 0) and (1, 1) for *ortho* and *para* states, respectively. CDs from Table IV were used to calculate lower rotational states, and in cases where there were redundant CDs the average value was used. The standard Watson-type effective Hamiltonian for an oblate symmetric top is the following:

$$\mathscr{H}^{W}_{rot} = B\mathbf{J}^2 + (C-B)J_z^2 - D_J\mathbf{J}^4 - D_{JK}\mathbf{J}^2J_z^2 - D_KJ_z^4 + H_J\mathbf{J}^6 + H_{JK}\mathbf{J}^4J_z^2 + H_{KJ}\mathbf{J}^2J_z^4 + H_KJ_z^6 + h_3(J_+^6 + J_-^6), \quad (1)$$

where h_3 is the off-diagonal sextic splitting term for symmetric tops with threefold symmetry, which is nonzero for $G = 3$ states. Least squares fits were performed using the software SPFIT developed by Pickett.[35] States were added incrementally in the order of increasing J, and when the rms error grew too large the parameter which improved the fit the most was included. The highest order parameters included in the fit were the sextic centrifugal distortion constants. If a state required octic or higher order terms, either the state was omitted or the relative energy from Lindsay and McCall was used instead, which had a larger uncertainty. Ultimately, 20 rotational states up to $(J, G) = (6, 5)$ were fit using 10 parameters with a reduced rms error of 1.11. Of the 18 relative energy levels, 10 were from the accurate newly determined values. The resulting molecular constants and predictions for the (1, 0) and (1, 1) energy levels relative to (0, 0) can be found in Table VI.

There are some concerns with using a Watson-type Hamiltonian to fit a "floppy" molecule. They require relatively large centrifugal distortion constants and successive terms in the expansion change sign, which can lead to truncation errors and poor convergence behavior. An alternative approach is to use an Euler-type Hamiltonian, which was derived by Pickett.[36] Euler's transformation can convert an alternating series to a series where all the terms have the same sign, while still converging to the same value. For an oblate symmetric top, this can be accomplished by replacing the angular momentum operators J_z^2 and $\mathbf{J}^2$ with the Euler functions J_z^{2*} and $\mathbf{J}^{2*}$. These have the form

$$J_z^{2*} = \frac{J_z^2}{1 + aJ_z^2 + b(\mathbf{J}^2 - J_z^2)}, \quad (2)$$

$$\mathbf{J}^{2*} = \frac{\mathbf{J}^2 - J_z^2}{1 + aJ_z^2 + b(\mathbf{J}^2 - J_z^2)}, \quad (3)$$

where a and b are transformation parameters. The Euler-type Hamiltonian is then

$$\mathscr{H}^{E}_{rot} = \sum_{i,j} X_{ij}(J_z^{2*})^i(\mathbf{J}^{2*})^j + h_3(J_+^6 + J_-^6), \quad (4)$$

where X_{ij} are the molecular constants. This can improve the convergence characteristics and the ability to predict the energy of unobserved states. Euler-type Hamiltonians have been successfully used to fit the isotopologues D_2H^+ and H_2D^+, and other molecules which suffer from poorly converging Watson-type Hamiltonians.[20,37–39]

The Euler functions are built into SPFIT, and the initial guesses for a and b were calculated using the Watson-type parameters as derived by Pickett.[36] The fit was approached in the same manner as the Watson-type fit by incrementally adding states and parameters, and limiting coefficients to the sextic order or lower. Then, the a and b transformation parameters were adjusted iteratively to achieve the best fit. This performed better than the Watson-type Hamiltonian, with 22 rotational states being fit with 9 parameters, and a reduced rms error of 1.12. Of the 20 relative energies, 12 were from the accurate newly determined values. The resulting molecular constants and calculated energy levels are also shown in Table VI. The results are in good agreement with the predictions from the Watson-type parameters, with the calculated energies of (1, 1) and (1, 0) differing by 2 and 8 MHz, respectively.

In order to ensure the chosen parameters were appropriate for predicting low lying energy levels, a test was devised. A new experimental data set was constructed from CDs where the energies of all $G = 2$ states were determined relative to (2, 2) instead of (1, 1), and all remaining *para* levels were calculated relative to (2, 1). This is as if the (1, 1) state were forbidden, and the $G = 2$ states were of a different spin species. Then, the parameters were used to fit the new

TABLE VI. Molecular constants from an Euler-type and Watson-type fit. All values are in MHz, and the 1σ uncertainties are given in parentheses in units of the least significant digit.

Parameter	Watson-type	Parameter	Euler-type
		$a \times 10^{-3}$	0.35
		$b \times 10^{-3}$	1.80
B	1 306 013.96(308)	$X_{01} = B$	1 306 024.20(204)
C	618 003.61(438)	$X_{10} = C$	617 993.57(231)
D_J	1 250.39(33)	X_{02}	1 096.683(217)
D_{JK}	−2 278.51(100)	X_{11}	1 354.34(66)
D_K	1 134.16(125)	X_{20}	108.897(192)
H_J	2.088 6(78)	X_{03}	2.152 5(55)
H_{JK}	−8.787(80)	X_{12}	−1.318(35)
H_{KJ}	11.856(224)	X_{21}	1.274(36)
H_K	−5.142(151)		
h_3	−0.218 4(44)	h_3	−0.207 74(144)
State	Predicted energy		Predicted energy
(1, 1)	1 922 439.0(44)		1 922 441.1(27)
(1, 0)	2 607 043.1(50)		2 607 051.1(33)

TABLE VII. Experimentally determined energy levels of H_3^+ rovibrational states relative to (0, 0). The energy levels were calculated from CDs, rovibrational transition frequencies, and the energies of (1, 1) and (1, 0) as determined by molecular constants.

$(J, G)u\|l$	Energy (MHz)	Energy (cm^{-1})
Ground state		
(1, 1)	1 922 441.1(27)	64.125 73(9)
(1, 0)	2 607 051.1(33)	86.961 86(11)
(2, 2)	5 075 561.1(81)	169.302 59(27)
(2, 1)	7 115 800.4(48)	237.357 55(16)
(3, 3)	9 454 074.6(66)	315.353 99(22)
(3, 2)	12 831 800.4(91)	428.022 79(29)
(3, 1)	14 832 773.2(74)	494.768 06(25)
(4, 4)	15 050 853.0(102)	502.042 41(34)
(3, 0)	15 495 739.9(77)	516.882 25(25)
(4, 3)	19 747 935.6(79)	658.720 23(25)
(4, 2)	23 038 282.9(103)	768.474 40(34)
(4, 1)	24 990 076.7(94)	833.579 23(31)
(5, 4)	27 850 004.6(116)	928.976 15(39)
(5, 3)	32 392 186.3(93)	1 080.487 03(31)
(5, 2)	35 588 431.6(118)	1 187.102 30(39)
(5, 0)	38 111 466.6(111)	1 271.261 69(37)
(6, 4)	42 891 749.4(129)	1 430.714 75(43)
(6, 3)	47 287 108.5(109)	1 577.328 16(36)
ν_2		
(1, 2)	76 392 298.8(112)	2 548.172 80(37)
(1, 1)	78 232 195.2(37)	2 609.545 14(12)
(2, 3)	78 374 281.2(73)	2 614.284 62(24)
(1, 0)	78 446 276.7(41)	2 616.686 13(13)
(3, 4)	81 528 373.8(116)	2 719.493 82(39)
(2, 2)	81 662 507.3(97)	2 723.968 04(32)
$(2, 1)l$	82 609 863.8(48)	2 755.568 45(16)
$(2, 1)u$	83 652 460.9(48)	2 790.345 74(16)
(2, 0)	84 327 427.7(33)	2 812.860 21(11)
(3, 3)	86 245 797.8(83)	2 876.850 15(27)
$(3, 2)l$	87 880 331.0(81)	2 931.372 31(27)
$(3, 2)u$	89 711 098.9(91)	2 992.440 15(29)
$(3, 1)l$	90 024 740.3(54)	3 002.902 10(18)
(3, 0)	90 715 994.1(86)	3 025.959 85(29)
$(3, 1)u$	91 840 646.5(85)	3 063.474 21(27)
(4, 4)	92 016 235.0(102)	3 069.331 21(36)
$(4, 3)l$	94 293 085.9(78)	3 145.278 79(25)
$(4, 3)u$	96 934 264.0(78)	3 233.379 01(25)
$(4, 2)l$	97 738 917.5(105)	3 260.219 36(35)
$(4, 1)l$	99 714 493.5(94)	3 326.117 48(31)
$(4, 2)u$	100 471 999.8(101)	3 351.385 17(34)
$(5, 4)l$	101 825 501.5(109)	3 396.533 12(39)
$(4, 1)u$	102 622 585.9(85)	3 423.121 00(27)
(4, 0)	103 339 935.5(86)	3 447.049 21(29)
$(5, 4)u$	105 231 784.6(109)	3 510.154 49(39)
$(5, 3)l$	106 526 370.9(95)	3 553.337 25(32)
$(5, 2)l$	109 734 426.5(118)	3 660.346 47(39)
$(5, 3)u$	110 142 653.1(91)	3 673.963 44(29)
(5, 0)	112 217 852.2(118)	3 743.184 63(39)
$(5, 2)u$	113 712 178.2(111)	3 793.029 98(37)
$(5, 1)u$	115 822 055.2(102)	3 863.407 91(34)
$(6, 4)l$	116 443 418.7(123)	3 884.134 35(43)
$(6, 3)l$	120 817 670.7(109)	4 030.043 70(36)
$2\nu_2^2$		
(2, 4)	150 867 809.0(48)	5 032.408 42(16)
(1, 2)	152 523 216.7(91)	5 087.626 88(29)
(2, 3)	155 328 183.2(52)	5 181.190 49(17)
(2, 2)	157 883 782.4(112)	5 266.436 10(37)
(2, 0)	158 497 901.5(63)	5 286.920 91(21)
(3, 4)	158 867 356.4(98)	5 299.244 60(33)
(3, 3)	162 821 175.1(92)	5 431.129 80(31)
(4, 5)	163 700 993.3(99)	5 460.477 37(33)
(3, 0)	166 906 399.7(77)	5 567.398 22(25)
(4, 4)	169 457 282.5(120)	5 652.486 51(40)
(5, 0)	191 623 790.5(111)	6 391.881 63(37)

relative energy levels, and the predictions of the (2, 1) − (1, 1) and (2, 2) − (1, 1) CDs were compared with the experimental values, which is analogous to calculating the (1, 0) and (1, 1) energy levels relative to (0, 0). Both parameter sets were found to behave satisfactorily, where predictions for the (2, 1) − (1, 1) and (2, 2) − (1, 1) CDs by the Watson-type parameters differed with the experimental values by −11(20) MHz and −2(19) MHz, respectively, while the predictions from the Euler type parameters differed by −3(11) MHz and 2(9) MHz.

In compiling a set of experimentally determined energy levels, the energies of the (1, 0) and (1, 1) states relative to (0, 0) were calculated using the Euler-type molecular constants, because of their overall better performance in fitting the ground state and predicting low lying energy levels. After this, CDs and transition frequencies were used to calculate the remaining energy levels. In cases where a state could be calculated with different sets of CDs or transitions, the average value was calculated. In total, 62 absolute energy levels were determined, with 18 in the ground state, 33 in the ν_2 state, and 11 in the $2\nu_2^2$ state with uncertainties of ~10 MHz. These can be found in Table VII.

2. Comparing theory and experiment

The accurate and precise experimentally determined energy levels can be directly compared with highly accurate calculations, which can reveal structure in the residuals that was previously hidden in the noise. Calculations are currently limited by the treatment of nonadiabatic coupling between electronic and nuclear motion, which is caused by electrons following the nuclei and increasing their effective mass.[5] The new experimental results can be used to closely assess the behavior of different approaches to this problem.

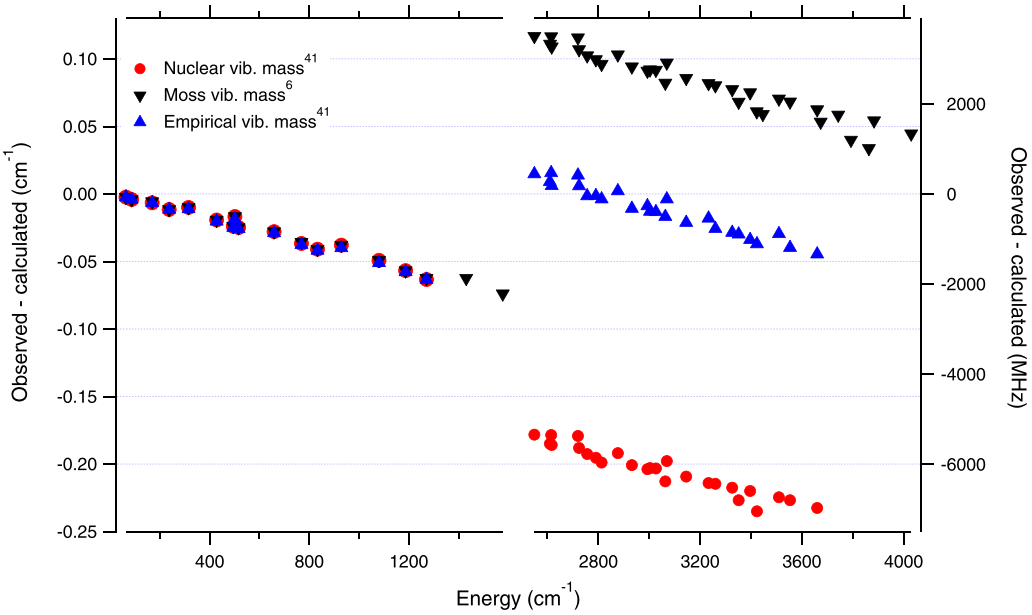

FIG. 4. The differences between the experimental energy levels and calculations which used nuclear rotational masses and different effective vibrational masses.[6,41]

A straightforward method for addressing nonadiabatic effects is to use motion-dependent masses for the vibrational and rotational terms in the kinetic energy operator. However, determining the appropriate effective masses from first principles is challenging. For H_2^+, Moss used a perturbative approach to calculate the effective vibrational mass,[40] which was larger than the nuclear mass (m_{nuc}) by approximately one half of the mass of an electron (m_e). When the Moss mass ($m_{nuc} + 0.475\,31 m_e$) was adopted for calculations of H_3^+, it improved agreement with rovibrational transition frequencies by a factor of two with an rms error of 0.101 cm^{-1}.[41] Mátyus *et al.* scaled the vibrational mass in order to achieve the best possible agreement with experimental transition frequencies and found a minimum at a lower effective mass of $m_{nuc} + 0.312\,24 m_e$.[41] This improved the agreement with experimental values by an order of magnitude to 0.008 cm^{-1}. However, when these results are compared with the experimentally determined absolute energy levels, the differences have an rms error of 0.026 cm^{-1}, which is indicative of a cancellation of error when compared with transition frequencies. A comparison between the experimental energy levels and calculations using nuclear, Moss, and empirically scaled vibrational

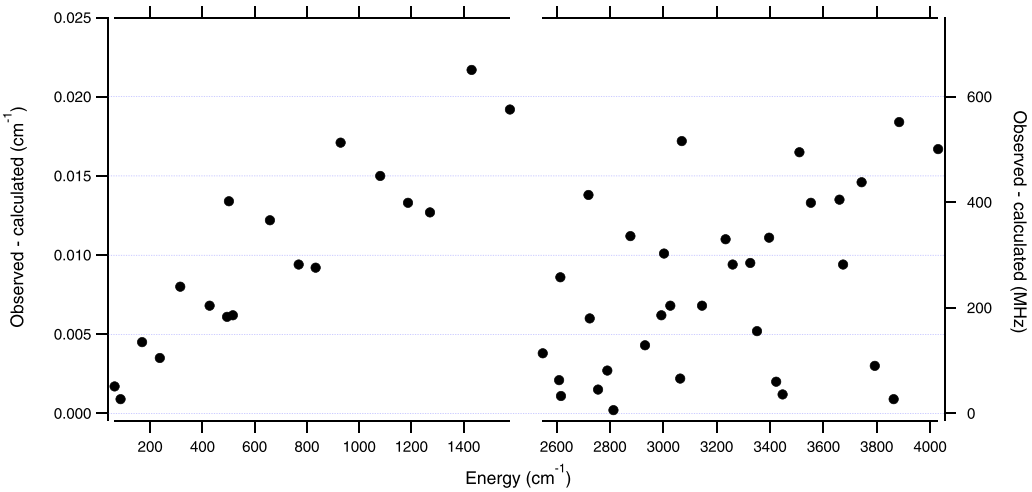

FIG. 5. The differences between the experimental energy levels and calculations which used scaled rotational and vibrational coordinate-dependent masses.[6]

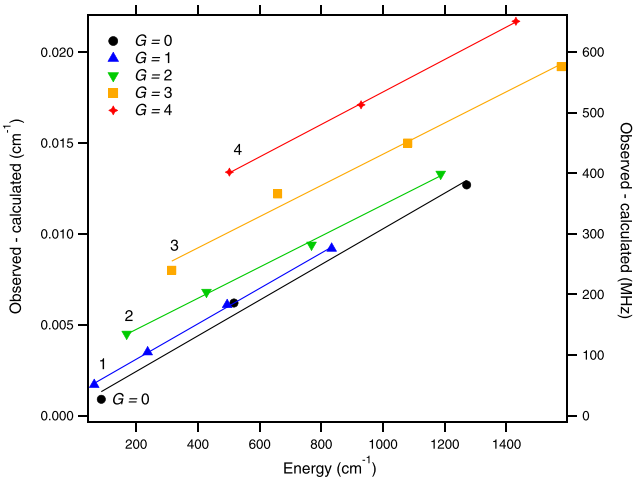

FIG. 6. A comparison between the experimental and calculated ground state energy levels using scaled rotational and vibrational coordinate-dependent masses,[6] with the G value of the state color coded. Linear fits of each G value are shown to demonstrate the G-dependent offset.

masses is shown in Fig. 4. Changing the effective vibrational mass shifts the offset of the ν_2 state, while in all three calculations, the disagreement changes with the rotational energy by approximately -1.5 MHz/cm^{-1}.

To address rotational contributions to the nonadiabatic coupling, Diniz *et al.*[6] calculated a coordinate-dependent rotational mass using an empirically derived formula. Additionally, coordinate-dependent vibrational masses were calculated using the Mullikan analysis of the electron density for the ground and ν_2 vibrational states. These surfaces were scaled using experimental transition frequencies to determine the effective rotational and vibrational masses, and a comparison between the results

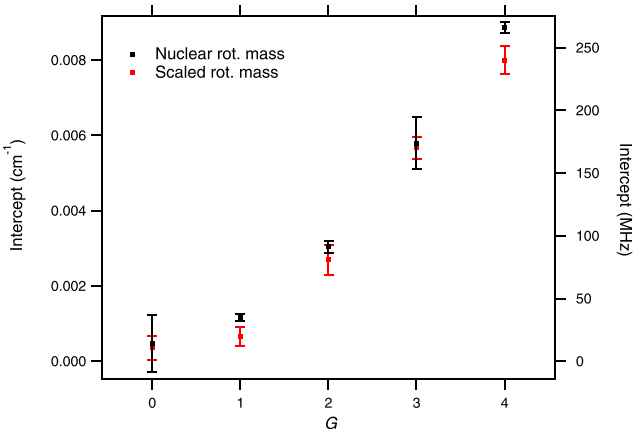

FIG. 7. The intercepts of the linear fits of the observed–calculated values for both scaled and nuclear rotational masses for different G values in the ground vibrational state.[6] The error bars are the uncertainty of the intercepts determined by the least-squares fits.

of Diniz *et al.* and the new experimentally derived energy levels is shown in Fig. 5. The effective masses both removed the offset of the ν_2 state and reduced the rotational energy dependence of the residuals to 270 kHz/cm^{-1}, resulting in an rms error of 0.01 cm^{-1}.

The accurate experimental rotational levels also reveal further structure in the residuals. In addition to the linear dependence of the disagreement on the state's energy, there is a clear dependence on G. Figure 6 shows the difference between the experimentally determined ground state energy levels and values calculated by Diniz *et al.*[6] The residuals of energy levels with the same G were fit to a line, and it was found that the slope was unaffected by the magnitude of G, while the intercept clearly increased with G. This trend also exists for calculations which use fixed masses, and Fig. 7 shows the intercepts of the linear fits for different G values from calculations using scaled and nuclear rotational mass. Despite the slopes of the two approaches being significantly different (-1.5 MHz/cm^{-1} and 270 kHz/cm^{-1}), the intercepts are quite similar, and both have a quadratic relationship with G. This could be due to the rotational nonadiabatic coupling having a dependence on the projection of angular momentum on the molecular axis, and this behavior cannot be captured by simply scaling the rotational mass of the nuclei. Although the general trend also exists for the ν_2 state, it is not as clear of an effect.

V. CONCLUSION

In this work, we report the results of a precise and accurate spectroscopic survey of H_3^+ rovibrational transitions in the $\nu_2 \leftarrow 0$, $2\nu_2^2 \leftarrow \nu_2$, and $2\nu_2^2 \leftarrow 0$ bands using the sub-Doppler technique NICE-OHVMS and frequency calibration with an OFC. Measurements spanned from 1.96 to 4.51 μm, and in total 53 transitions had their uncertainties improved by more than an order of magnitude. These are the first sub-Doppler measurements of H_3^+ overtone and hot band transitions, which allowed for accurate and precise determination of energy level spacings in the ground state using CDs, including between states with $\Delta G = \pm 3$. This in turn allowed for the direct prediction of 16 forbidden rotational transitions with uncertainties of approximately 10 MHz. This includes the transition (4, 4) $\rightarrow$ (3, 1) which is a possible astrophysical maser, and the improved frequency of this transition opens up a new avenue for the astronomical detection of H_3^+.

Ground state molecular constants were determined by fitting the relative energy levels to an effective Hamiltonian, which were used to calculate the energies of the lowest *ortho* and *para* levels relative to the forbidden (0, 0) level. This allowed for 62 accurate rovibrational energy levels to be determined through CDs and rovibrational transition frequencies. These results were compared with accurate *ab initio* calculations, and the residuals revealed dependence on G which could not be discerned with comparisons to previous experimental measurements. As theorists continue to develop new strategies for addressing nonadiabatic effects for this fundamental molecular system, the results from this work will provide valuable experimental benchmarks.

SUPPLEMENTARY MATERIAL

See supplementary material for additional information on the asymmetry of the NICE-OHVMS line shapes, the transitions which contributed to each CD, and the files related to the SPFIT analyses.

ACKNOWLEDGMENTS

C.R.M. is grateful for support from the National Aeronautics and Space Administration Earth and Space Science Fellowship (Grant No. NESSF NNX16AO86H). The authors wish to acknowledge James N. Hodges and Adam J. Perry for their contributions throughout much of the project. Additionally, the authors thank Philip A. Kocheril, Anne Marie Esposito, and Alex W. Schrader for their assistance in data collection. This work was also funded by the National Science Foundation (Grant No. PHY 14-04330).

REFERENCES

[1] J. Tennyson, J. Chem. Phys. **145**, 120901 (2016).
[2] N. Indriolo, T. R. Geballe, T. Oka, and B. J. McCall, Astrophys. J. **671**, 1736 (2007).
[3] P. Drossart, J.-P. Maillard, J. Caldwell, S. J. Kim, J. K. G. Watson, W. A. Majewski, J. Tennyson, S. Miller, S. K. Atreya, J. T. Clarke, J. H. Waite, Jr., and R. Wagener, Nature **340**, 539 (1989).
[4] M. Pavanello, L. Adamowicz, A. Alijah, N. F. Zobov, I. I. Mizus, O. L. Polyansky, J. Tennyson, T. Szidarovszky, and A. G. Császár, J. Chem. Phys. **136**, 184303 (2012).
[5] J. Tennyson, O. L. Polyansky, N. F. Zobov, A. Alijah, and A. G. Császár, J. Phys. B: At., Mol. Opt. Phys. **50**, 232001 (2017).
[6] L. G. Diniz, J. R. Mohallem, A. Alijah, M. Pavanello, L. Adamowicz, O. L. Polyansky, and J. Tennyson, Phys. Rev. A **88**, 032506 (2013).
[7] P. Jusko, C. Konietzko, S. Schlemmer, and O. Asvany, J. Mol. Spectrosc. **319**, 55 (2016).
[8] H.-C. Chen, C.-Y. Hsiao, J.-L. Peng, T. Amano, and J.-T. Shy, Phys. Rev. Lett. **109**, 263002 (2012).
[9] J. N. Hodges, A. J. Perry, P. A. Jenkins II, B. M. Siller, and B. J. Mccall, J. Chem. Phys. **139**, 164201 (2013).
[10] Y.-C. Guan, Y.-H. Chang, Y.-C. Liao, J.-L. Peng, L.-B. Wang, and J.-T. Shy, J. Chem. Phys. **148**, 124310 (2018).
[11] B. M. Siller, M. W. Porambo, A. A. Mills, and B. J. McCall, Opt. Express **19**, 24822 (2011).
[12] A. J. Perry, J. N. Hodges, C. R. Markus, G. S. Kocheril, and B. J. McCall, J. Mol. Spectrosc. **317**, 71 (2015).
[13] J. T. Hougen, J. Chem. Phys. **37**, 1433 (1962).
[14] C. M. Lindsay and B. J. McCall, J. Mol. Spectrosc. **210**, 60 (2001).
[15] R. W. P. Drever, J. L. Hall, F. V. Kowalski, J. Hough, G. M. Ford, A. J. Munley, and H. Ward, Appl. Phys. B **31**, 97 (1983).
[16] C. R. Markus, A. J. Perry, J. N. Hodges, and B. J. McCall, Opt. Express **25**, 3709 (2017).
[17] C. R. Webster, J. Opt. Soc. Am. B **2**, 1464 (1985).
[18] B. J. McCall, "Spectroscopy of H_3^+ laboratory and astrophysical plasmas," Ph.D. thesis, University of Chicago, 2001.
[19] P. A. Kocheril, C. R. Markus, A. M. Esposito, A. W. Schrader, T. S. Dieter, and B. J. McCall, J. Quant. Spectrosc. Radiat. Transfer **215**, 9 (2018).
[20] C. R. Markus, P. A. Kocheril, and B. J. McCall, J. Mol. Spectrosc. **355**, 8 (2019).
[21] A. J. Perry, C. R. Markus, J. N. Hodges, G. S. Kocheril, and B. J. McCall, in the 71st International Symposium on Molecular Spectroscopy, Urbana, IL, 2016.
[22] C. R. Markus, P. A. Kocheril, A. M. Esposito, A. W. Schrader, and B. J. Mccall, in the 73rd International Symposium on Molecular Spectroscopy, Urbana, IL, 2018.
[23] A. R. W. McKellar and J. K. G. Watson, J. Mol. Spectrosc. **191**, 215 (1998).
[24] W. A. Majewski, M. D. Marshall, A. R. W. McKellar, J. W. C. Johns, and J. K. G. Watson, J. Mol. Spectrosc. **122**, 341 (1987).
[25] M. G. Bawendi, B. D. Rehfuss, and T. Oka, J. Chem. Phys. **93**, 6200 (1990).
[26] J. K. G. Watson, S. C. Foster, A. R. W. McKellar, P. Bernath, T. Amano, F. S. Pan, M. W. Crofton, R. S. Altman, and T. Oka, Can. J. Phys. **62**, 1875 (1984).
[27] D. Uy, C. M. Gabrys, M.-F. Jagod, and T. Oka, J. Chem. Phys. **100**, 6267 (1994).
[28] W. H. Flygare, Acc. Chem. Res. **1**, 121 (1968).
[29] B. M. Dinelli, S. Miller, and J. Tennyson, J. Mol. Spectrosc. **153**, 718 (1992).
[30] L.-W. Xu, C. Gabrys, and T. Oka, J. Chem. Phys. **93**, 6210 (1990).
[31] F.-S. Pan and T. Oka, Astrophys. J. **305**, 518 (1986).
[32] J. H. Black, Faraday Discuss. **109**, 257 (1998).
[33] T. Furtenbacher and A. G. Császár, J. Quant. Spectrosc. Radiat. Transfer **113**, 929 (2012).
[34] I. I. Mizus, A. Alijah, N. F. Zobov, L. Lodi, A. A. Kyuberis, S. N. Yurchenko, J. Tennyson, and O. L. Polyansky, Mon. Not. R. Astron. Soc. **468**, 1717 (2017).
[35] H. M. Pickett, J. Mol. Spectrosc. **148**, 371 (1991).
[36] H. M. Pickett, J. C. Pearson, and C. E. Miller, J. Mol. Spectrosc. **233**, 174 (2005).
[37] S. Brünken, H. S. P. Müller, F. Lewen, and T. F. Giesen, J. Chem. Phys. **123**, 164315 (2005).
[38] S. Brünken, H. S. P. Müller, C. Endres, F. Lewen, T. Giesen, B. Drouin, J. C. Pearson, and H. Mäder, Phys. Chem. Chem. Phys. **9**, 2103 (2007).
[39] P. Jusko, M. Töpfer, H. S. P. Müller, P. N. Ghosh, S. Schlemmer, and O. Asvany, J. Mol. Spectrosc. **332**, 33 (2017).
[40] R. E. Moss, Mol. Phys. **89**, 195 (1996).
[41] E. Mátyus, T. Szidarovszky, and A. G. Császár, J. Chem. Phys. **141**, 154111 (2014).